Turbulence experiments in the swash zone

Marco Petti [a,*], Sandro Longo [b,1]

[a] *Dipartimento di Georisorse e Territorio, Università degli Studi di Udine, Via del Cotonificio, 114, 33100 Udine, Italy*
[b] *Dipartimento di Ingegneria Civile, Università degli Studi di Parma, Parco Area delle Scienze, 181/A, 43100 Parma, Italy*

Abstract

Turbulence and water surface elevation measurements were carried out in the swash zone which was induced by plunging and collapsing breakers in a wave flume. Three different period regular waves were generated on a $1/10$ smooth impermeable concrete beach and the water surface elevations were collected by a number of wave gauges and a run-up meter lying on the bottom. Velocity measurements were carried out by a Laser Doppler velocimeter system, at spatial steps of 1 mm from the bottom, along three vertical sections in the swash zone.

The data have been used to describe the wave front dynamics, to derive the length and velocity macro and micro scales and the Eulerian frequency spectrum. In some points, it shows a double structure.

The results add to and expand on similar results obtained by other researchers in the surf zone. © 2001 Elsevier Science B.V. All rights reserved.

Keywords: Swash zone; Breaking waves; Turbulence; Length scales; Coastal hydrodynamics

1. Introduction

The swash zone is the part of the beach that is alternately dry and covered by water due to the wave run-up. The morphology and evolution of natural beaches are strongly affected by swash hydrodynamics; swash zone dynamics also play a major role in defining the proper boundary conditions for detailed models that aim to describe the wave motion up to the intersection with the beach.

A complete analysis of swash zone hydrodynamics requires turbulence analysis and quantification. Turbulence, mainly generated by breaking waves and partially by bottom friction, is clearly an important phenomenon in this region, being closely related to wave evolution and sediment transport. Large-scale turbulence also influences the flow geometry.

Turbulence analysis starts with the description of its scales, usually based on measured velocity time series; unfortunately measurements in the swash zone are quite difficult because the fluid motion is often a two-phase fluid flow (three phases if sediments are present), with air trapped during breaking and convected down to the bottom. LDV, PIV and hot probe measurements are inhibited in these conditions. Even the splitting of the measured velocity into 'mean motion' and 'turbulent component' is quite compli-

---

* Corresponding author. Tel.: +39-0432-558-712; fax: +39-0432-558-700.
E-mail addresses: marco.petti@uniud.it (M. Petti), slongo@unipr.it (S. Longo).
[1] Tel.: +39-0521-905-157; fax: +39-0521-905-924.

cated and far from an easy matter. The first problem is the definition of turbulence in an oscillatory flow, i.e. what is the turbulence frequency range and how to extract it from measurements.

There have been several attempts to classify turbulence after breaking into one of two main categories, 'free turbulence' and 'wall turbulence', because it is easier to study new phenomena by comparison with known phenomena. Several experiments using LDV, PIV and other flow visualisation techniques have given useful information. Peregrine and Svendsen (1978) modelled the flow field as a turbulent mixing layer, with turbulence spreading toward the wave crest and the bottom, and a long wake behind the breaking region in which the turbulence decays; the surface roller is only a small part of the region of highly turbulent flow and acts as a trigger to initiate the turbulence. Recent experiments by Kozakiewicz et al. (1998) on externally generated turbulence influence on a turbulent oscillatory boundary layer, show that the transition occurs earlier, with a smaller phase difference between the free stream velocity and the bed shear stress than in the absence of external turbulence; the wave friction tends to increase from 50% to 100% of the friction in the absence of external turbulence, with an increased apparent bottom roughness.

The measurements of Battjes and Sakai (1980) on the velocity field underneath the breaker generated by a hydrofoil positioned at some distance below the water surface in a steady current indicated that the flow has many aspects of a wake flow, with turbulence scale decreasing with the square root of the distance and lateral length scale increasing with the square root of the distance downstream from a reference point.

Recently, flow visualisation techniques revealed the existence and the importance of large-scale eddies depending on geometry: Nadaoka et al. (1989) found that two families of coherent structures exist, described as 'horizontal eddies' and 'obliquely descending eddies'. The first family has axis parallel to the wave crests while the second family is formed of eddies having a principal axis aligned to that of the mean strain rate, being the most effective in extracting energy from the mean flow. They assumed the co-existence of a rotational and irrotational velocity fields, the first due to 'eddies', the second due to

'waves', and separated the two fields using experimental data. The eddies carry vorticity and travel near the surface at a slower velocity than the wave celerity, enhancing the mass and momentum transport and globally smoothing the wave profile relative to the expected wave profile for a simple traditional irrotational wave field.

Some of the above experiments represent an idealisation of the real conditions, even though they are quite effective in separating the different aspects of the dynamics and in stating some reference points for the global analysis of the real phenomenon.

Experiments in more realistic conditions are becoming available: Flick and George measured velocity in the surf and swash on a natural beach, using hotfilm anemometers. They found that in the surf zone the length scales are proportional to the water depth (or equivalently to the local bore or wave height); in the swash zone, the length scales are proportional to the distance from the bottom.

Measurements on macro turbulence using 3D velocity component instruments were carried out in the field by Rodriguez et al. (1999), with the identification of temporal and spatial scales of macro vortices under spilling/plunging breaking waves. Rodriguez et al. found that horizontal eddies are more significant than 3D or vertical eddies, at least in the inner surf zone, with an almost uniform distribution of the kinetic turbulent energy along the vertical in the swash zone. The magnitude of the horizontal length integral scale (computed using the spatial correlation of the velocity component in the horizontal plane) tends to increase from $\approx 20\%$ of the mean water depth in the outer surf zone to $\approx 60\%$ in the inner surf zone.

Information on the vertical integral length scale after breaking is given in Pedersen et al. (1998). The spatial cross correlation was computed using two LDVs sampling the vertical velocity components; the first kept at a fixed level above the bottom, the second moved at different points along the vertical. The integral length scale increases from the bed to a value of 30% of the local still water depth.

An extensive study on turbulence under spilling and plunging breakers is given in Ting and Kirby (1994, 1995, 1996). They found that the turbulence dynamics are strongly influenced by the breaker type, with mean flow transport of kinetic energy

seaward under the spilling breaker and shoreward under the plunging breaker.

The general framework of dynamics in the swash zone is still not clear and several points need to be discussed and focused. The purpose of the present study is to analyse fluid velocity and free surface elevation measurements in the swash zone, where both turbulence generated by the breaker and at the bottom are present, including the wave front dynamics at the intersection with the beach. Our investigation expands on similar investigations on surf zone turbulence with more difficulties due to the severe experimental conditions: even in the laboratory, with enhanced importance of surface tension effects, the fluid after breaking comprises water and air bubbles making LDV measurements difficult; for the most shoreward section fluid is absent for more than 50% of the time.

The adopted experimental set-up and procedure is described in Section 2; Section 3 presents the time series analysis and Section 4 includes a general discussion on time dependent turbulence, in order to state the general problem and the approximations needed to render it manageable. The experimental results are presented and discussed in Section 5.

2. Experimental set-up and procedure

The experiments were conducted in a wave flume 48 m long, 0.8 m wide, and 0.8 m deep, built completely of steel and glass. At one end of the flume a wave maker is installed, which consists of a paddle moved by an electronic-controlled hydraulic system. The mechanical structure, which supports the paddle, allows it to work as a piston, flap, or cradle type: in the present experiments a piston-type was used. The displacement of the paddle is controlled by a hydraulic servo-valve moved by a computer system through an electric low voltage signal; a feedback checks and regulates the paddle displacement. The computer that controls the generation-acquisition system is a desktop equipped with an Intel 80586 processor, two boards A/D and D/A 12 bit converters, and one analogue low pass filter. A high-level software (Petti, 1988, 1994) programmes the runs of the waves in the flume, shows in real time data collected and stores the signals coming from 32 acquisition channels connected with as many gauges. An integrated software performs a second order wave generation, to minimise spurious waves.

A concrete beach sloping at 1:10 was constructed in the flume starting 37.5 m from the paddle; its surface was finished in order to reduce its roughness. Three specimens have been collected above the maximum water level, assuming that the wave action is not strong enough to smooth the surface. The geometric scale of the roughness has been evaluated through a detailed analysis of the specimens using a Laser interferometric pick-up transverse unit (RTH Form Talysurf-120L), according to ISO 4287. The average height of the crests is around 30 μm without evident differences among the specimens; the bottom surface is quite regular, without apparent 3-D effects induced on the wave field.

Water levels were measured by a series of 12 wave gauges: four movable, at different positions along the flume and eight fixed located in the surf and swash zone (Fig. 1).

Three of the four movable gauges (1 to 3) were placed on the plane bottom portion of the flume, at distances from the paddle of 8.5, 23 and 37.5 m; their output was used to check the generated waveforms. The fourth movable wave gauge was positioned at 39.2 meters from the wave paddle. Eight fixed gauges (5 to 12) were placed at intervals of 20 cm (this was the best compromise to avoid reciprocal interference and to cover the measured zone with an adequate resolution) across the swash zone.

The wave gauges used consist of twin parallel wire ($\phi = 0.3$ mm) meters; the resistance between the wires, converted to output voltage, is acquired by the acquisition system that converts the signal to water level elevation based upon a calibration curve. The characteristic voltage versus water level, if the field around the wires is homogeneous and symmetrical, is linear. During tests, the linearity and the stability of wave gauges were periodically checked repeating, whenever necessary, the calibration steps. The level of electric noise, evaluated as the standard deviation of the output signal in still water conditions, corresponds to a maximum error in water level of $\Delta\eta = \pm 1$ mm with a transient error in dynamic conditions, partially due to surface tension effects, included in this value. Particular attention was given to the calibration of the gauges in the swash zone,

| water depth [cm] | 8 | 6 | 4 | 2 | 0 | −2 | −4 | −6 | | −30 | −40 | −40 | −40 |
| distance from the paddle [m] | 42.3 | 42.1 | 41.9 | 41.7 | 41.5 | 41.3 | 41.1 | 40.9 | | 39.2 | 37.5 | 23.00 | 8.50 |

run–up meter ⑬   ⑫⑪⑩⑨⑧⑦⑥⑤   wave gauges   ④   ③   ②   ①
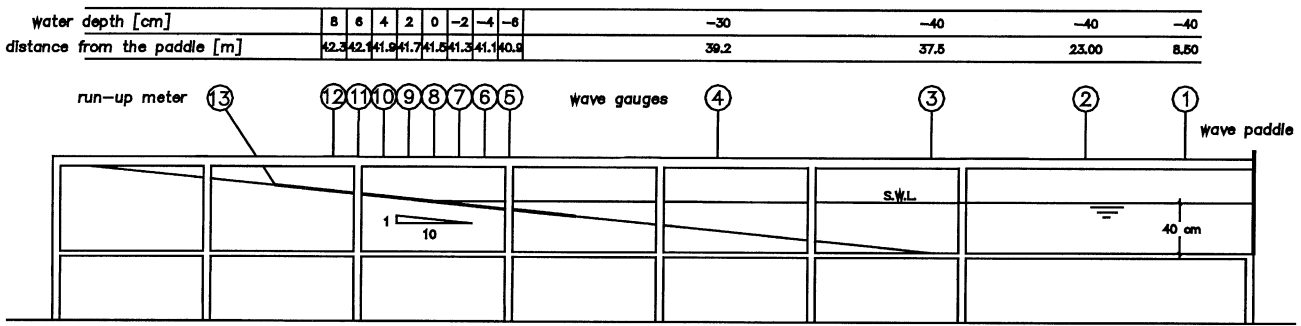
wave paddle

1 / 10

S.W.L

40 cm

Fig. 1. Experimental set-up and location of wave gauges.

which is characterised by an uprush/backrush cycle with the gauges wet only for a fraction of the wave period.

A run-up meter (gauge 13) was placed parallel to the bottom in the swash zone, to measure the bore front position. It consists of twin wires oriented parallel to the bottom, encompassing the entire swash range. With such a configuration, the system loses the symmetry characteristics of the electromagnetic field because of the presence of the bottom layers. Placing the wires too close to the beach causes an excessive signal error due to meniscus effects (meniscus between the bottom and the wires) and of an additional resistance induced by the concrete of the bottom. If the wires are too far from the beach, the signal improves but a systematic geometrical error is introduced, as sketched in Fig. 2. A good compromise was found by placing the wires at a fixed distance of 5 mm (along the vertical) from the bottom. To correct the systematic geometrical error, a video camera was used, comparing the position of the bore front as detected by video images with the position recorded by the run-up meter.

As a consequence of the effects discussed above the typical calibration curve of the run-up meter was non-linear, thus a fifth order polynomial function was necessary to fit its calibration curve to make the non-linear error equal to the other gauge errors.

Instantaneous velocities have been measured in the swash zone by a forward scatter LDV system, at several points equally spaced at 1 mm along the vertical starting at 0.5 mm from the bottom and in three different sections. The three sections (Fig. 3) were at the still water level intersection with the slope (mid section), 20 cm shoreward (upper section), and the last at 20 cm seaward (lower section). The position of the upper section was reduced to $+5$ cm for the shorter waves, in order to measure the velocity signal for a sufficiently long enough time.

The Laser Doppler used was a He–Ne 30 mW system with a measurement volume that is an ellipsoid whose axes are of the order of 1 mm. The Doppler frequency information was collected by a photomultiplier, elaborated by a frequency tracker and stored by the acquisition system. The error in velocity measurements is 1% of the selected frequency range.

The main problem with LDV measurements in the swash zone is related to the periodic backrush: the absence of water, or simply air bubbles crossing through the measurement volume, unlock the signal. The locking–unlocking sequence is not strictly predictable, even in the presence of regular wave trains; for this reason we selected the valid signal using an algorithm defining a Boolean function (equal to one if the signal is valid and zero otherwise). The overall results have been checked and corrected, whenever necessary, by visual observation of the raw time series plots (Fig. 4).

A digital videocamera was used for qualitative preliminary analyses of the breaking process and field of motion, run-up and run-down height estimates (correction and calibration of the run-up meter), the location of the breaking point and assessments of breaking wave height.

Three regular wave trains were generated in the flume, leaving enough time between two successive tests in order to establish quiescent water conditions.
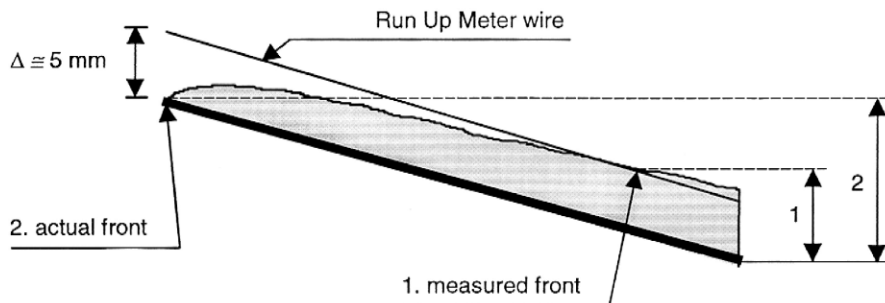

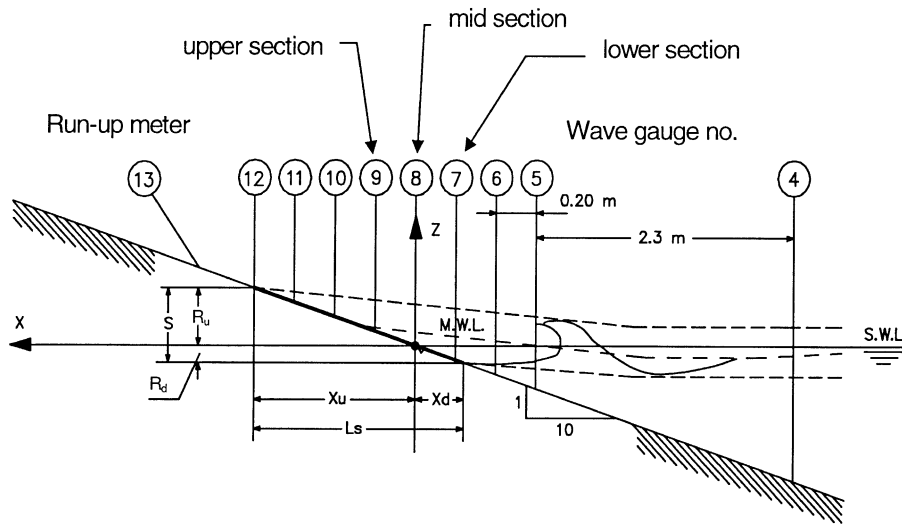Fig. 2. Systematic error in run-up meter measurements.

Fig. 3. Location of the wave gauges in the surf and swash zone.

The whole set of regular wave tests performed is summarised in Table 1; subscript 1 refers to data collected at gauge 1, subscript 0 refers to deep-water conditions evaluated by linear wave theory.

Velocity measurements at several points required many runs for each regular wave, thus a repetitiveness analysis was carried out. This was done successfully by checking the wave height and wave
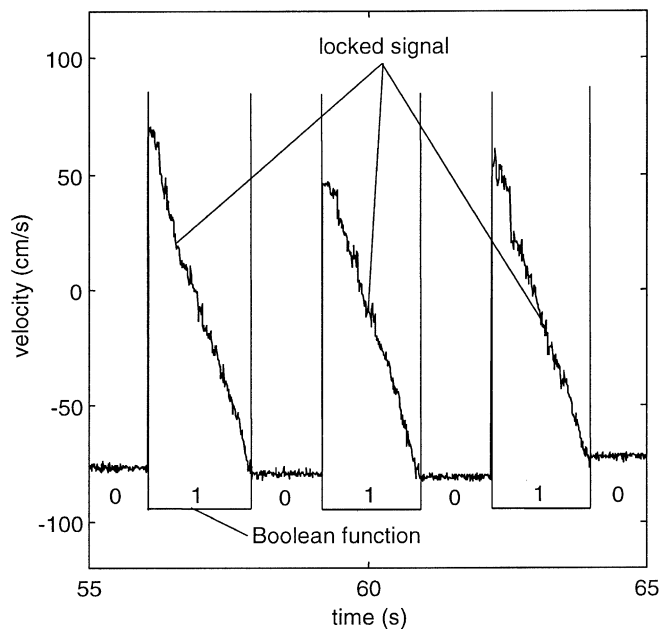

Fig. 4. LDV signal selection.

Table 1
Regular waves generated

Test	H_0 (cm)	H_1 (cm)	T (s)	H_0/L_0	ξ_b	I_b	Breaking type
RH040T20	3.6	3.5	2.0	0.0057	0.93	0.43	Plunging
RH040T25	3.3	3.5	2.5	0.0034	1.12	0.36	Plunging
RH040T30	3.3	3.8	3.0	0.0024	1.28	0.31	Collapsing

period collected by gauges 1, 2 and 3 for the whole set of tests. Using data evaluated in deep water, accounting for the shoaling effect, surf similarity parameters ξ_b and I_b were estimated for each wave train (Gourlay, 1992) by the relations:

$$\xi_b = \frac{1.45\tan(\vartheta)}{(H_0/L_0)^{0.36}}, \quad I_b = \frac{1}{2.5\xi_b}. \quad (1)$$

For the whole set of tests, the sampling rate was 100 Hz and the data acquisition time was 600 s. A detailed report of the experiments is in Petti et al. (1998).

3. Time series analysis of periodic signals

The definition of turbulence in a non-stationary flow field, with the presence of a mean oscillatory flow and several effects such as macro turbulence induced oscillations, is far from easy. Many authors have proposed different methods, mostly based on the concept of filtering the time series using different shapes of filters. The most commonly used process is ensemble averaging, adopted in similar processes analysis by (Stive, 1980; Ting and Kirby, 1994, 1995, 1996; Pedersen et al., 1998). As pointed out in the last reference, ensemble averaging (often defined as phase averaging) requires the phenomenon to be highly reproducible, otherwise a general dampening and a distortion of the output occur. This method is almost useless for non-periodic signals. The ensemble or phase average $\tilde{\eta}(t)$ of a time series is expressed as:

$$\tilde{\eta}(t) = \frac{1}{N}\sum_{k=0}^{N-1}\eta(t+kT) \qquad 0 \leq t < T, \quad (2)$$

where $\eta(t)$ represents instantaneous values, N is the number of waves in the chosen time interval and T is the period. This operator is highly sensitive to small fluctuations of the period, due for example to a frequency modulating effect.

If a well-identified trigger is available, the conditional average is expressed as (Blackwelder and Kaplan, 1976):

$$\tilde{\eta}(t) = \frac{1}{N}\sum_{k=0}^{N-1}\eta(t+t_k) \qquad 0 \leq t < \min(T), \quad (3)$$

where t_k is the instant of trigger of the k-cycle and $\min(T)$ is the minimum time period in the series of N cycles. The conditional average is widely used in studying burst phenomena once they have been detected and is widely known as the Variable Interval Time Average (VITA). A more correct and unbiased result can be obtained stretching the data of each cycle (the time period of each cycle, equal to $(t_k - t_{k-1})$ is not constant) before averaging in order to extend it all over the mean period. Such a technique is equivalent to the demodulation process in the time-domain of a weak-modulated (in frequency) signal.

Another well-known operator is the moving average, able to concentrate on a localised region in time:

$$\langle\eta(t)\rangle = \frac{1}{T_m}\int_t^{t+T_m}\eta(t^*)\mathrm{d}t^*, \quad (4)$$

with T_m the period of time averaging.

If the value of time series is not defined during some time intervals (e.g. Eulerian fluid velocity is strictly related to mass presence in the point of measurements, and is not defined during mass absence) we can define a phasic average:

$$\hat{\eta} = \frac{\sum_i \int_{\Delta T_i}\eta(t)\mathrm{d}t}{\sum_i \Delta T_i}, \quad (5)$$

where ΔT_i are the time steps during water presence. This last operator is particularly important in the analyses of our data because in some sections of measurements the water is often absent.

For completeness, the well-known time average operator is reported:

$$\langle \eta \rangle = \frac{1}{T} \int_0^T \eta(t)\,\mathrm{d}t, \qquad (6)$$

with T the period of time averaging.

All the above-defined operators are linear and can be applied in sequence without rank.

4. Time dependent turbulence

Turbulence is quite a complicated phenomenon and a deterministic description is not presently known. Moreover, in respect to most modelled physical situations, in swash zone dynamics we are dealing with a turbulence time dependence, with a definition of unsteady turbulent flow which is in itself challenging: turbulence is essentially described as random, rotational and three dimensional, dissipative and time varying. The subtle difference between time varying and time dependent refers to the existence of unsteadiness developed inside the flow field or externally imposed. The two motions, i.e. the erratic unsteady instabilities and the organised external imposed fluctuations, coexist and often overlap and interact. A useful tool is the triple decomposition (Hussain, 1983), with a generic time dependent variable decomposed into a mean value, an organised component and a fluctuating component (see Telionis (1981), for a detailed analysis, and McComb (1990), for discussion), but it generates impressive equations involving several correlation terms.

A substantial improvement in turbulence modelling has been obtained by means of the analysis of scales involved, essentially a length and a velocity scale. Thus, turbulence modelling is split into velocity scale and length scale modelling.

The velocity scale U is often expressed as the root mean square fluctuating velocity, i.e. turbulence energy κ:

$$U \equiv \sqrt{\kappa} = \sqrt{\frac{1}{2}\widetilde{u_i' u_i'}}. \qquad (7)$$

The summation rule is assumed in Eq. (7) and the symbol $\sim$ means ensemble average in the classical sense.

The length scale L is often expressed as the integral length scale Λ based on the spatial correlation function:

$$\Lambda = \int_0^\infty R(r)\,\mathrm{d}r \qquad (8)$$

where:

$$R(r) = \frac{\widetilde{<u'(x)u'(x+r)>}}{\widetilde{<u'^2(x)>}} \qquad (9)$$

is the spatial correlation function for homogenous and isotropic turbulence.

The eddy viscosity, having the dimension of the product of a length scale by a velocity scale

$$\nu_\mathrm{T} = LU, \qquad (10)$$

is a measure of the efficiency in transferring momentum by random fluctuations of velocity in the presence of shear rate. For a time dependent flow field, as in the swash zone, the scales can be either the averaged values over a cycle or time dependent (phase averaged) values, giving a pseudo steady or time varying eddy viscosity. In the present analysis, we follow the former approach, reconstructing as many terms as possible in the balance equations using the experimental results.

Referring to experiments, it is usually easier to measure fluid velocities at a single point obtaining a time series of the local velocity, which leads to the Eulerian time correlation:

$$R_E(\tau) = \frac{\widetilde{<u'(t)u'(t+\tau)>}}{\widetilde{<u'^2(t)>}}. \qquad (11)$$

The hypothesis of a stationary flow field holds in Eq. (10). Consequently, the integral time scale is defined as:

$$T_\mathrm{E} = \int_0^\infty R_\mathrm{E}(\tau)\,\mathrm{d}\tau, \qquad (12)$$

i.e. the area under the time autocorrelation function, assumed as the duration of the macro vortices. The
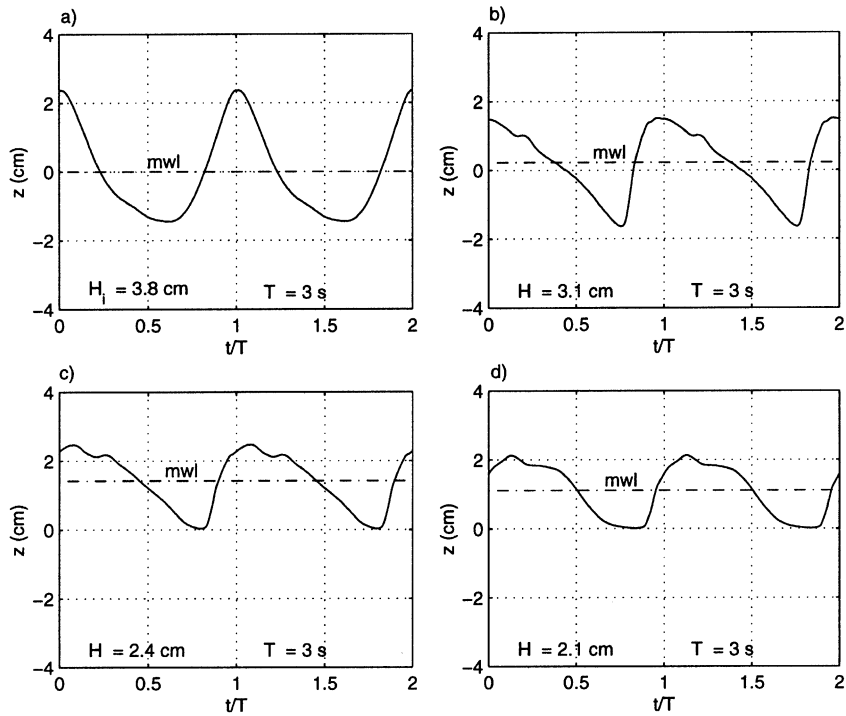
Fig. 5. Phase-averaged surface elevations $\tilde{\eta}(t)$: (a) Section 1, (b) Section 7 (lower), (c) Section 8 (mid), (d) Section 9 (upper).
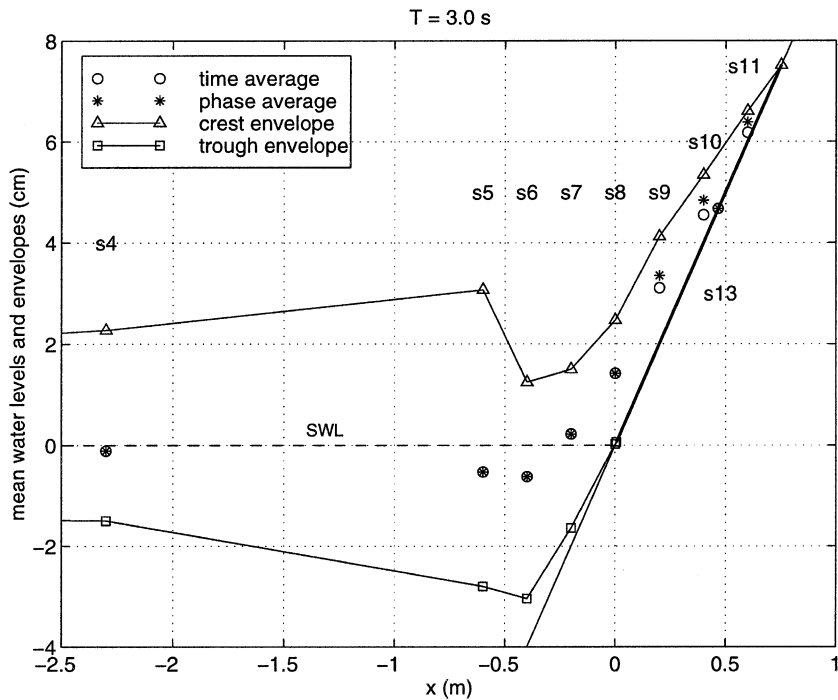

Fig. 6. Test RH040T30: Set up and set down profiles, crest and trough envelopes.

Table 2
Crest celerity

Section	Measured crest celerity (m/s)	H (cm)
T = 3 s		
7 (lower)	0.43	3.5
8 (mid)	1.33	2.5
9 (upper)	1.17	2.5
T = 2.5 s		
7 (lower)	0.40	3.5
8 (mid)	0.58	2.0
9 (upper)	1.05	2.0
T = 2 s		
7 (lower)	0.37	3.9
8 (mid)	0.62	1.9
9 (upper)	0.74	1.5

transformation of the integral time scale into the integral length scale can be carried out assuming Taylor's hypothesis of "frozen turbulence":

$$\frac{\partial}{\partial t} \approx -U\frac{\partial}{\partial x} \qquad (13)$$

where U is a proper velocity scale. Taylor's hypothesis represents a zero-order Lagrangian approximation, in the sense that the fluid particle displacement is related only to the pure translation of the vortex within which it is trapped, neglecting the effects of rotation of the vortices and of acceleration. This hypothesis is valid if the ratio between the fluctuating velocity and the mean velocity is less than ~ 0.1 and is better satisfied at a high wave number; for all the tests it was observed that the ratio of a turbulence estimator $\left\langle \sqrt{\widetilde{u'^2}} \right\rangle$ and the amplitude of the periodic velocity components $\tilde{u}$ is very close to 0.1 and Taylor's hypothesis was applied.

5. Experimental results

5.1. Water surfaces and front dynamics

We first focus on the free surface elevation measured at several sections and on the toe kinematics of the bore. Mean water levels $\tilde{\eta}(t)$, $\tilde{\eta}$ and $\langle \tilde{\eta} \rangle$ were estimated for each test at each wave gauge to obtain the variations in the free surface and the set-up profile. Fig. 5 plots some phase averaged $\tilde{\eta}(t)$ surface elevations for a wave period of $T = 3.0$ s; the breaking takes place at Section 5.
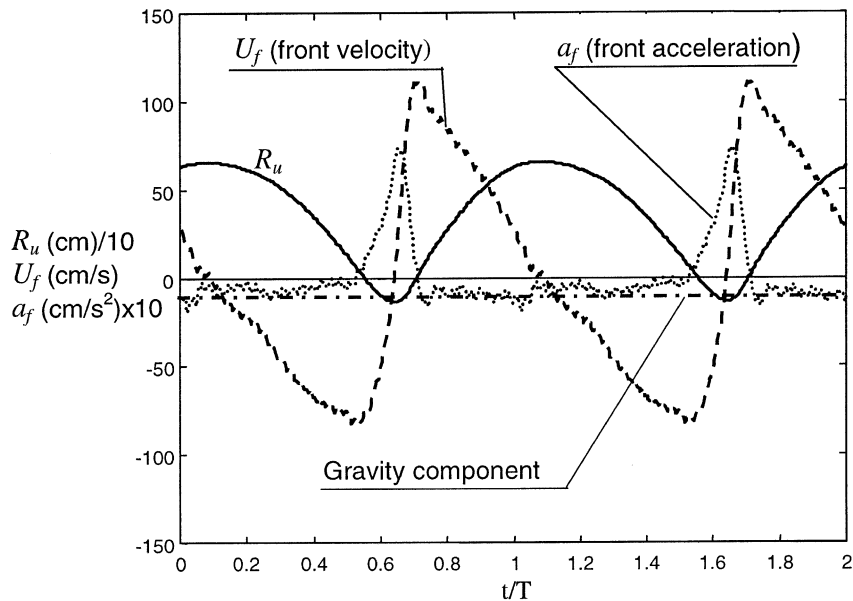

Fig. 7. Front position (R_u), velocity (U_f) and acceleration (a_f). The dash dot line is the gravity component. $T = 3$ s.
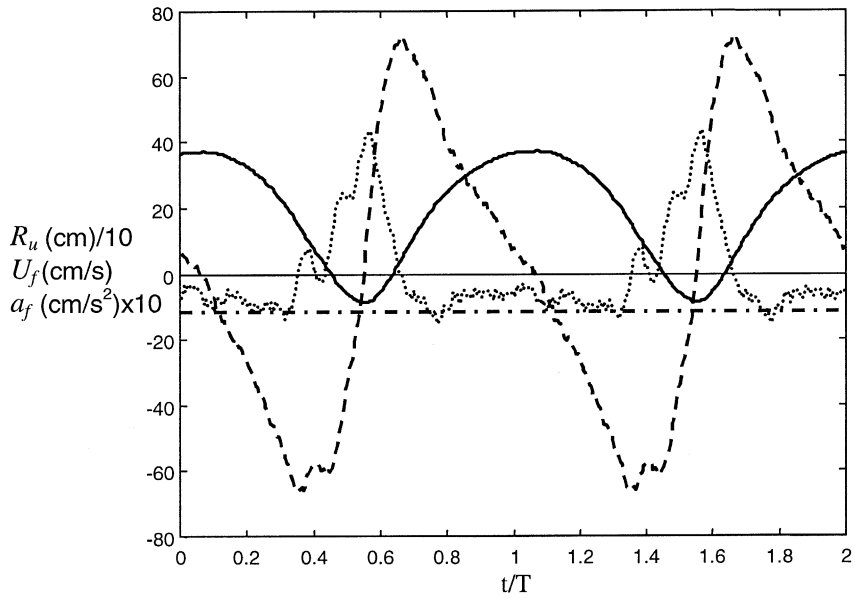
Fig. 8. Front position, velocity and acceleration. $T = 2.5$ s. For caption see Fig. 7.

Fig. 6 plots the phase averaged $\tilde{\eta}$ and the time averaged $\langle \tilde{\eta} \rangle$ surface elevations in all the measurement sections for a wave period of $T = 3.0$ s. The dashed lines represent the crest and trough envelopes. Time and phase averages are coincident in the sections where water is always present; the phase
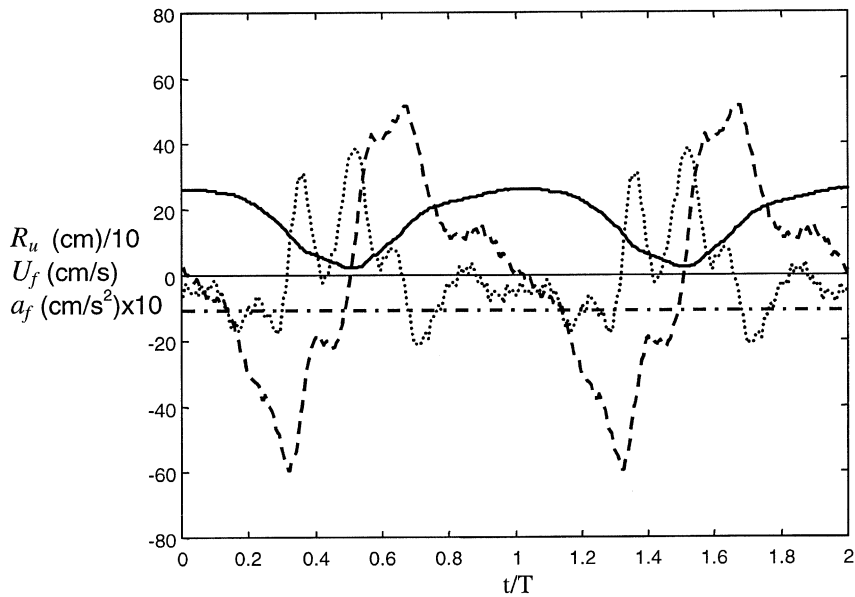
Fig. 9. Front position, velocity and acceleration. $T = 2$ s. For caption see Fig. 7.

average is higher than the time average where the fluid is not present. Their ratio is a measure of the fluid mean concentration.

After breaking, the wave changes its shape and it is not formally correct to define phase celerity. Nevertheless, it is possible to evaluate the propagation speed of the crest by measuring the phase lag of the maximum water level at the current section of interest with that of the previous section, as reported in

Table 2. In general, we found a propagation speed of crests higher than theoretical bore celerity because of the strong initial pressure gradient which accelerates the fluid; the friction effects also play an important role in decelerating the fluid motion. The balance between these two terms depends on the breaker type, as discussed in the following.

The kinematics of the toe of the front were obtained from the run-up meter signal: the velocity and
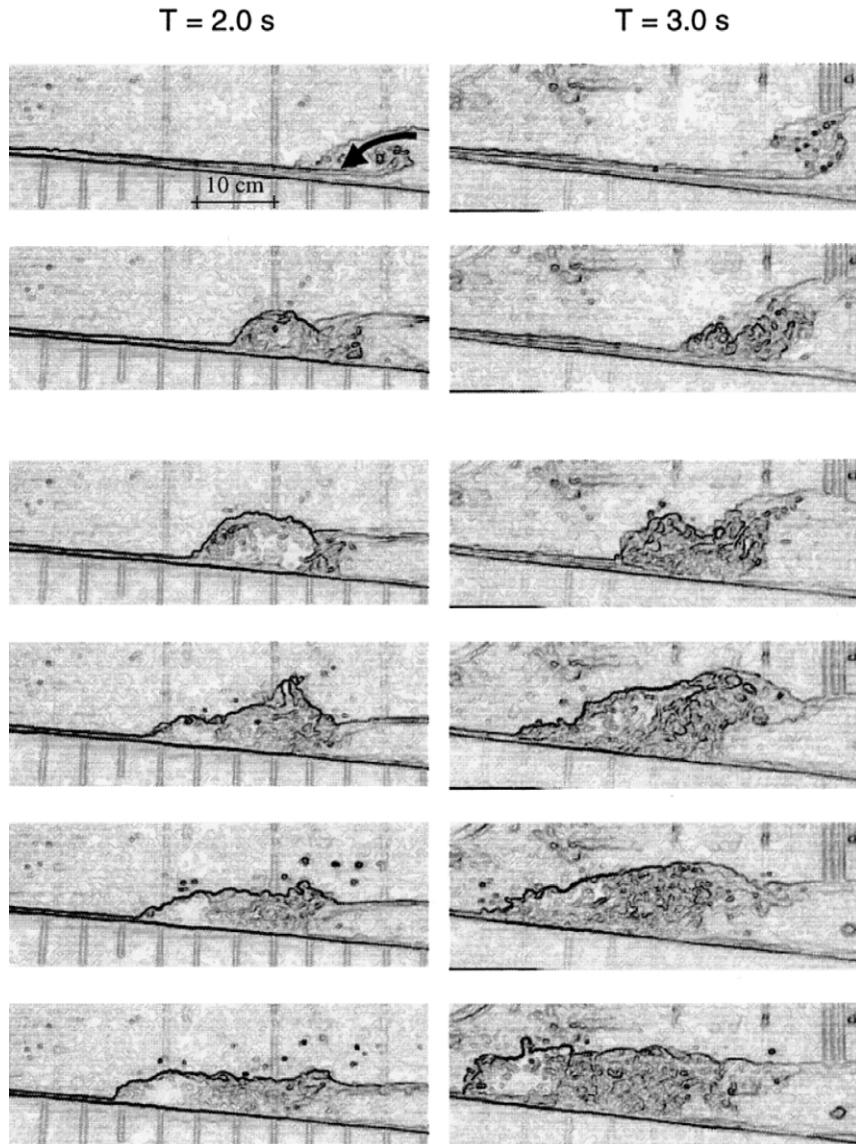

Fig. 10. Frame sequences at the breaking for tests $T = 2$ s and $T = 3$ s (time step $2/25$ s).

the acceleration were computed through numerical differentiation and filtering, and are reported in Figs. 7–9. The front velocity has a maximum of about 1 m/s during fast acceleration (when the roller arrives) for the 3-s wave; the correspondent acceleration is about 10 times the gravity component parallel to the bottom. The initial front velocity is comparable with the front velocity in a dam break on a dry horizontal bottom, equal to $2\sqrt{gH}$ (Stoker, 1957). The process of front acceleration and deceleration is monotonic for the 3- and 2.5-s waves, whereas there is a secondary peak for the lower period wave of 2-s. It is the structure of the breaker that modifies the efficiency of pushing the water uprush and creates the secondary peak, due to pulsation of the momentum flux and pressure gradient; the smaller period wave tends to break as plunging, with higher velocity component normal to the bottom and a higher relative dissipation. The larger period waves tend to collapse but they are sufficiently organised after breaking to efficiently cause uprush. This mechanism is clearly evident in the frame sequence reported in Fig. 10 for the lowest and the highest wave period. Following Shen and Meyer (1963) the maximum run-up height is simply equal to $R_{u} = U_0^2/2\,g$, which is a total conversion of kinetic energy to potential energy, where U_0 is the initial front velocity and g is gravity. For the three waves the theoretical maximum run-up, obtained assuming for U_0 the peak values (Figs. 7–9), are equal to 6.2, 2.4 and 1.8 cm, while the measured maximum run-up are equal to 6.5, 3.9 and 2.4 cm. The measured run-up is greater than the predicted and, of course, cannot be attributed to dissipation effects, which act to reduce the run-up relative to the theoretical.

A possible interfering phenomenon is the presence of water due to backrush when the bore is climbing. Its presence is strictly related to the ratio between the period of swash and the wave period. The water body landward of the breaker can be modelled as an oscillator subject to external periodic force. For a run-up with initial velocity U_0, the period of oscillation is equal to $T_s = 2U_0/g\sin\theta$ where θ is the bottom slope. Assuming the front velocity at the run-down level as the initial velocity, we compute a period of oscillation equal to ≈ 2.25 s, ≈ 1.4 and ≈ 1.2 s for the three waves of 3, 2.5 and 2.0 s, respectively, indicating that there is no apparent interference between the incoming bore and the back flow. This is consistent with the video and the experimental results except for the 3-s wave period. For this wave period, the level of organisation of motion is quite high and is able to generate a significant extra run-up, as also indicated by the fast crest (see Table 2); the measured swash period is close to the wave period and thus interaction is
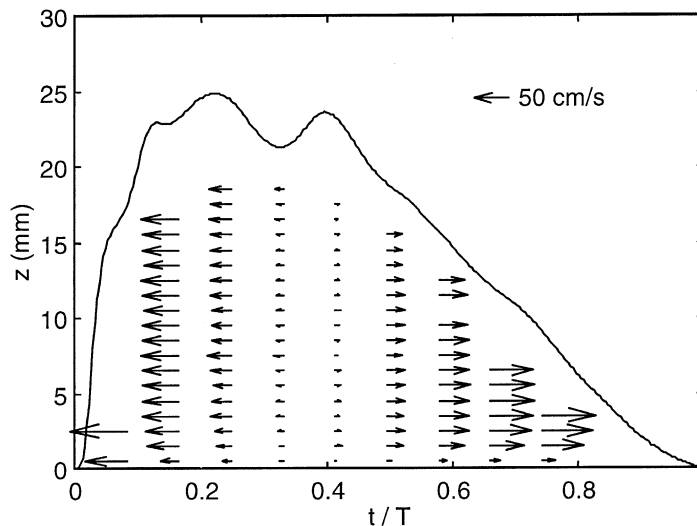

Fig. 11. Mean velocity $\tilde{u}(z,t)$ in the mid section; $T = 3$ s.

expected. The interaction between backrush and up-rush seems also to influence the spectrum of turbulence, as shall be discussed in Section 5.3.

5.2. Mean motion and turbulence under breaking waves

The turbulence effects on fluid motion in the swash zone after breaking in plunging and collapsing are quite evident in the frame sequence reported in Fig. 10.

The air–water jet after breaking is essentially directed along the normal to the bottom; it partially rebounds on the bottom, with strong dissipation, and globally gives a small contribution to the flux of momentum in the stream direction; then the fluid stream arrives and washes it. The dynamics are quite similar to those depicted by Peregrine (1983) and Yeh et al. (1989), with a bore essentially exchanging momentum with the small body of water in front of it instead of suddenly collapsing. The interaction between the incoming stream and the splashed jet, transformed in a large vortex, generates free surface oscillations directed seaward and entrains the bubbles of the jet.

The interactions are quite strong at the initial contact, but continue, due to the linear and angular momentum difference present in the two bodies. The result is a series of smaller rollers that follows the main roller, with a progressively reduced size. The presence of such secondary rollers is evident in all videos and is detected in the free surface elevation spikes in the sections after the breaking section, i.e. Sections 6, 7, 8 up to 11 (only results for Sections 7, 8 and 9 are reported in Fig. 5). Near the maximum run-up, only a small quantity of bubbles remains or simply has been convected to the water surface, while most of the rest have been eliminated.

The reference scheme is the one depicted by Nadaoka et al. (1989). The main difference for our experimental condition is the limiting water depth under the breaker; while in Nadaoka et al. experiments, the turbulent bore generated after a spilling-type breaker moved over a water cushion of more than 10 times its height, in the present experiments the bore itself moves over an initially almost dry bottom. Turbulence probably does not have enough space to organise itself in diagonal vortices, parallel

to the shear rate, and is essentially convected with the front.

During uprush the eddies fill the fluid domain, interacting with the bottom and partially with the backrush fluid motion if present (it was not in the present tests except for the 3-s wave period), while the potential flow field is almost absent. During backrush, most of the external generated vorticity and turbulence has been damped and turbulence generation is almost completely controlled by the bottom.

Phase averaged velocity profiles $\tilde{u}(z,t)$ were calculated at each level from the bottom in the three
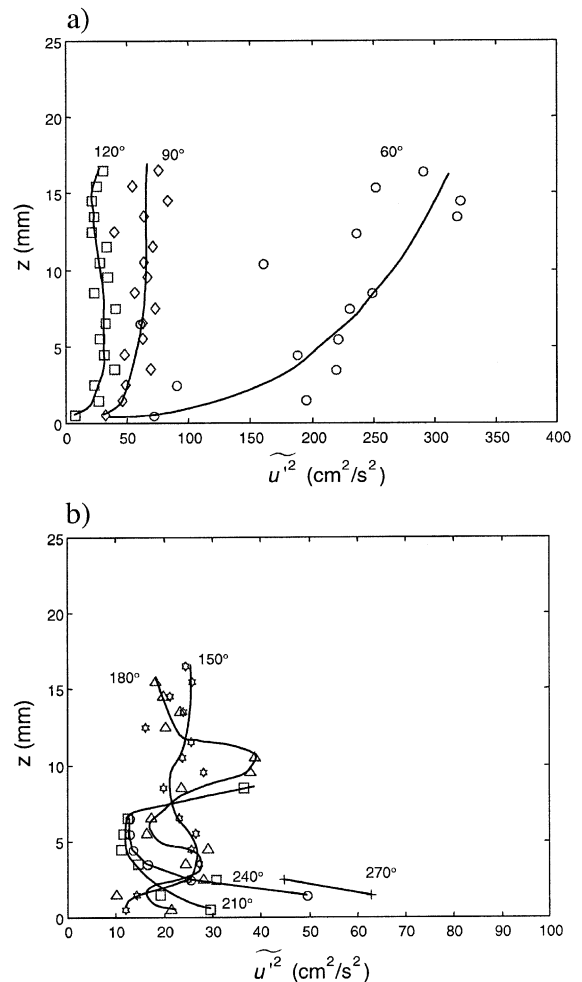

Fig. 12. Turbulent energy at different phases. (a) uprush, (b) backrush. $T = 3$ s, mid section.

Sections 7 (lower), 8 (mid) and 9 (up). Turbulent oscillations $u'(z,t)$ along the main flow direction have been obtained by subtracting the phase-averaged value $\tilde{u}(z,t)$ from the instantaneous velocity measured by LDV $u(z,t)$:

$$u'(z,t) = u(z,t) - \tilde{u}(z,t). \qquad (14)$$

The phase averaged values were obtained using a VITA technique triggering to the local minimum water level. Fig. 11 plots the vector velocities $\tilde{u}(z,t)$ obtained for a test with $T = 3$ s at different phases. Figs. 12–14 show the turbulent energy profiles at different phases in the mid section for the three
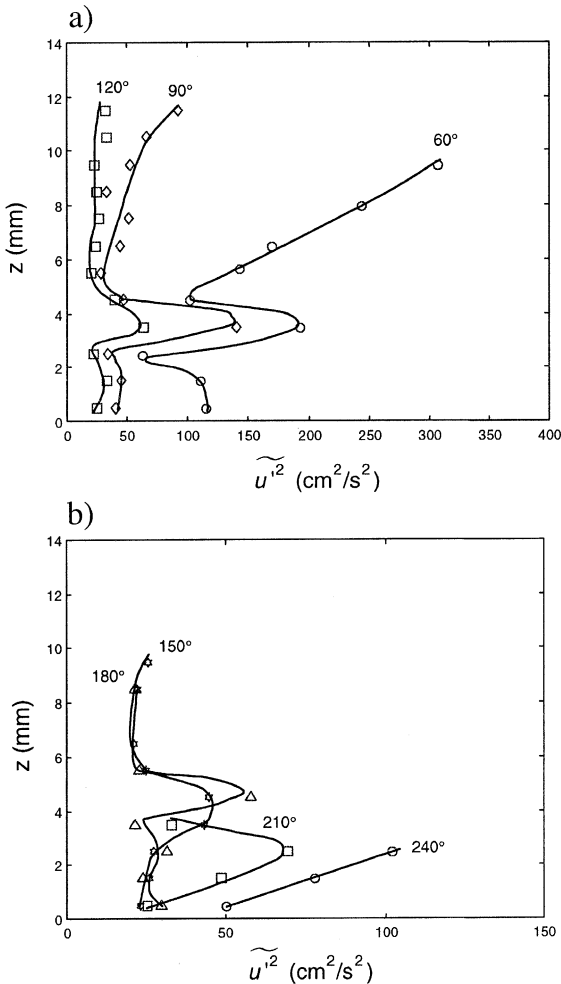

a)

b)

Fig. 13. Turbulent energy at different phases. (a) uprush, (b) backrush. $T = 2.5$ s, mid section.
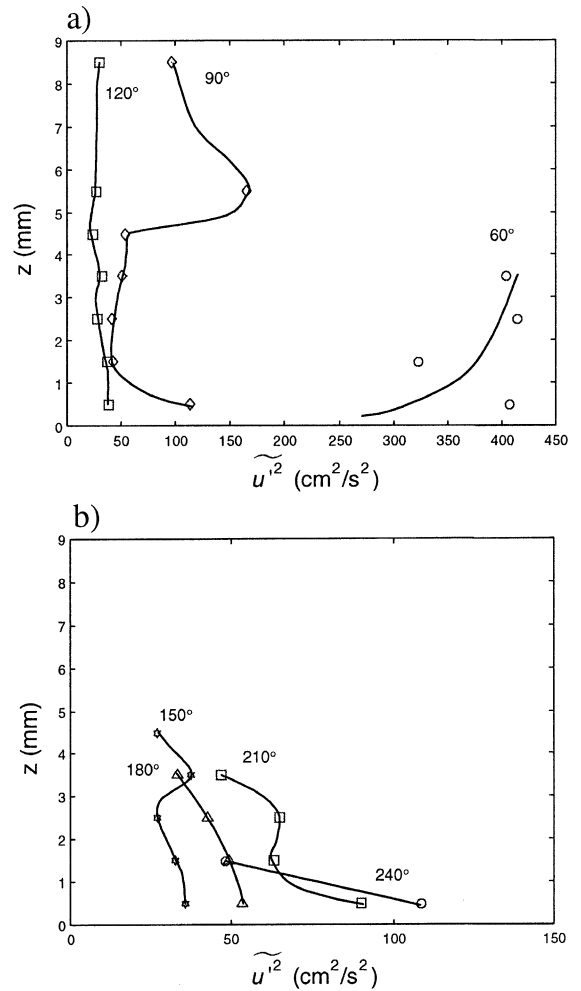

Fig. 14. Turbulent energy at different phases. (a) uprush, (b) backrush. $T = 2$ s, mid section.

regular waves, separating uprush and backrush. Velocity is almost uniform along the vertical during uprush, even though a small overshoot can be detected with a maximum at decreasing height level over the bottom for a decreasing wave period (not presented).

The first phases of the motion, as well as the last, are not detectable because of the strong bubble presence and the consequent unlocking of the LDV. The changing flow direction in the mid section is between 120° and 150°, with a shift towards higher values of the phase for shorter wave periods. The uprush is driven by the strong roller that develops on

breaking, whereas down rush is essentially gravity driven: the bottom turbulent boundary layer grows progressively with a smoother and more regular velocity profile. The turbulent energy profiles clearly show that a strong difference exists between the two phases: during uprush turbulence is generated by the roller near the free surface and dominates the whole flow field. The decay time is relatively small and it takes only a small fraction of the period to dissipate most of its energy. As pointed out by Ting and Kirby (1994), the short decay time is due to the presence of macro vortices, whose 'turnover time' is of the order of Λ/U (Tennekes and Lumley, 1972) being Λ the macro length scale and U a velocity scale (e.g. the amplitude of the phase averaged velocity). Large values of velocity scale induce small duration of the vortices and fast decay of turbulence. A simple estimation gives $t = 0.05$ s for $U = 0.5$ m/s and $\Lambda = 2$ cm, i.e. less than $10°$ in phase for all the three wave periods. A high residual value of turbulence is still present near the free surface at $90°$. Note that some of the turbulent energy profiles strongly resemble measurements in hydraulic jumps, obtained at a distance of 7 times of the entry depth from the toe of the roller (Resh and Leutheusser, 1972).

The phase averaged turbulent energy flux due to the mean motion in the main direction is reported in

Fig. 15 for the 3-s wave period. The maximum shoreward flux is in the mid section for all the periods (not presented), indicating that even though the turbulent energy level is higher in the lower section, the nearest section to the breaker, higher efficiency and organisation is reached in the mid section; in the upper section the energy level (not presented) is substantially reduced and the resulting turbulent energy flux is reduced.

5.3. Turbulence scales and frequency spectra

Using the definitions and assumptions introduced in Section 4, length macro scales were calculated assuming for U the velocity $\langle \sqrt{\tilde{u}^2} \rangle$, and are reported below in Fig. 16.

Results are non-dimensional with respect to the maximum local water depth δ instead of the usual still water depth or the mean water depth. This choice was made because in the swash zone the mean water depth is usually very low, and its influence on the phenomena appears to be very limited.

The measured length scales are generally higher than those found in an open channel (dotted lines) and have an evident maximum near the bottom at $z/\delta \approx 0.1$. In an open channel the maximum is
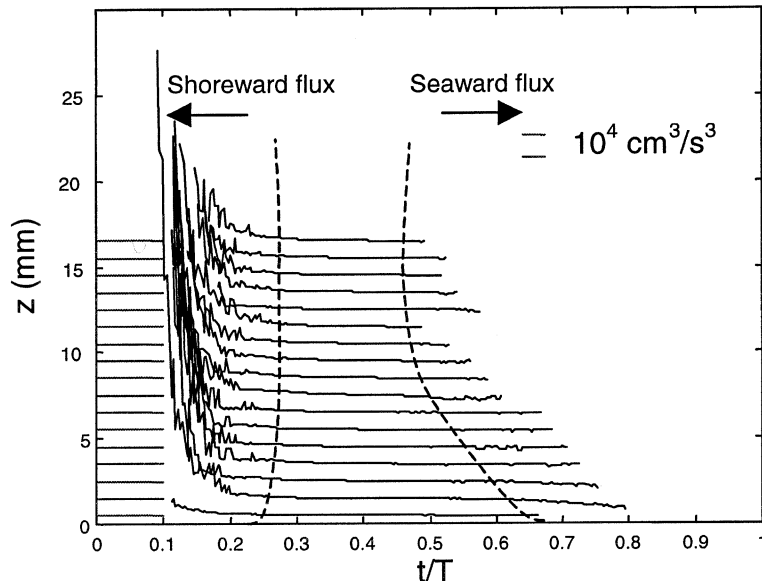

Fig. 15. Turbulent energy flux $\widetilde{\tilde{u}u'u'}$ in the mid section. $T = 3$ s.
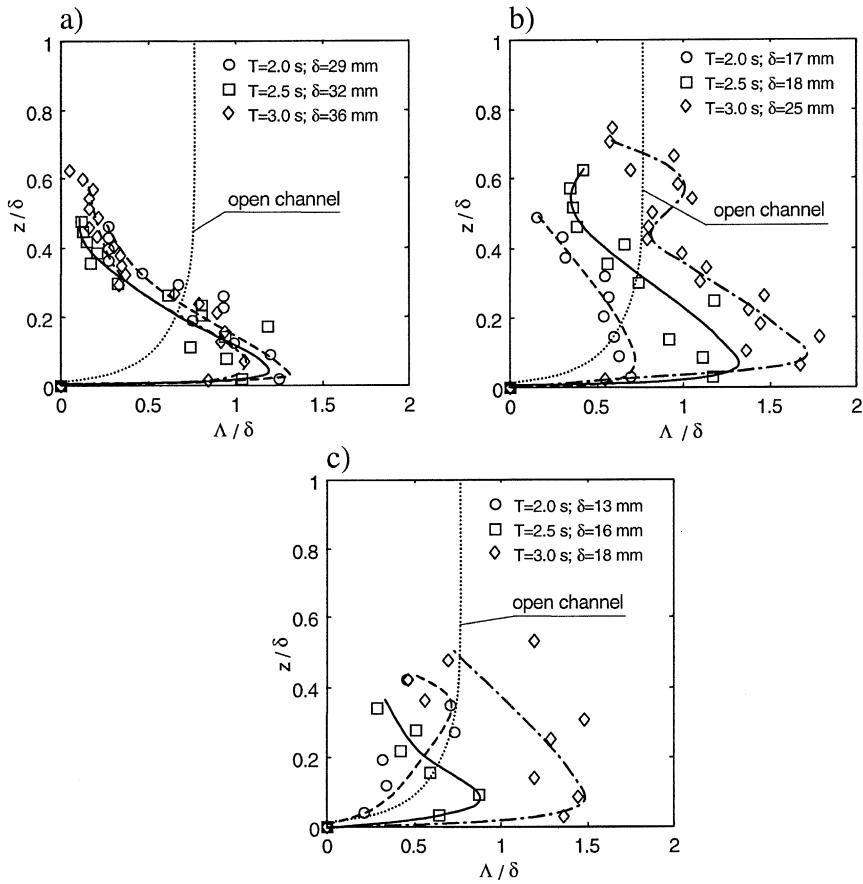
Fig. 16. Length macro scale Λ estimated for all waves: (a) the lower section (7), (b) mid section (8) and (c) upper section (9), as a function of non-dimensional depth.

around 0.6 h (h is the water depth) and the macro length scales depend slightly on the Reynolds number based on friction velocity and water depth, but are substantially independent of wall roughness (Nezu and Nakagawa, 1993). The length macro scales have similar profiles for all the three waves in the lower section (Fig. 16a), indicating that the macro vortices are not yet dispersed. In this section the length macro scale can be expressed as $\Lambda/\delta \approx 25\ z/\delta$ for $z/\delta < 0.05$, $\Lambda/\delta \approx 0.06(z/\delta)^{-1}$ for $z/\delta > 0.05$. In the mid and upper sections, macro vortices have smaller non-dimensional size for shorter wave periods. In the upper section the macro vortices structure for the wave period $T = 2$ s resembles the structure in an open channel. The high values near the bottom can be interpreted as the effect of the anisotropy.

The time micro scale, i.e. the time scale of the vortices where most energy is dissipated, can be obtained from the interception of the time axis with the parabola osculating the autocorrelation function in its vertex:

$$\tau_E = \sqrt{\frac{-2}{\left[d^2 R_E / dt^2\right]_{t=0}}} \ . \qquad (15)$$

Because of a major uncertainty in computing the parabola on the basis of the discrete autocorrelation function, using few points near the vertex, it is computationally better to calculate $-d^2 R_E/dt^2$ as the autocorrelation of the derived process du'/dt (Papoulis, 1965), even though the numerical compu-
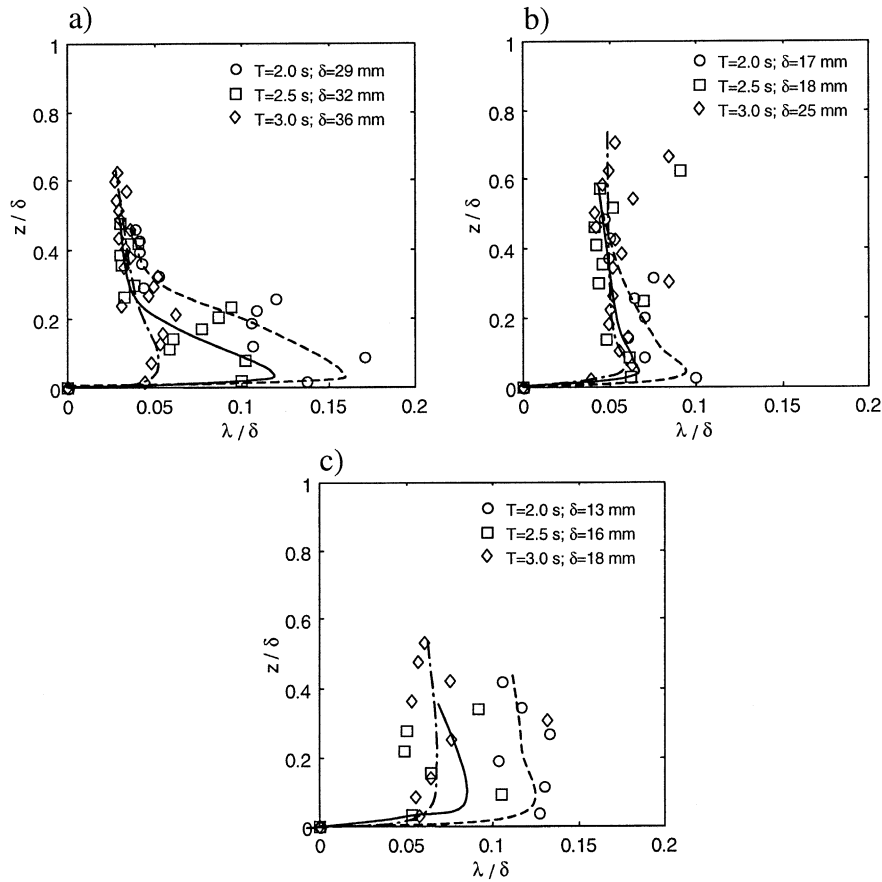
Fig. 17. Taylor length micro scale λ vs. height level estimated for all waves: (a) lower section (7), (b) mid section (8) and (c) upper section (9).

tation of time derivatives partially overcomes the advantage of using the complete time series. Typical autocorrelation functions R_E have an exponential decay.

Similarly, assuming for U in Eq. (13) the velocity scale $\left\langle \sqrt{\widetilde{u'^2}} \right\rangle$ based on turbulence, the Taylor length micro scale was computed as:

$$\lambda = \left\langle \sqrt{\widetilde{u'^2}} \right\rangle \tau_E; \qquad (16)$$

and are reported below in Fig. 17.

In the application of Eq. (13) the choice of a velocity U different from the organised motion velocity has been made to avoid some inconsistencies arising with flow fields having zero, or almost zero,

mean velocity (as the periodic flow field under analysis). We are computing the time averaged autocorrelation (and all the derived function, as the length scales and the spectra), without phase resolving the process. A crude application of Eq. (13) would give an undefined spatial derivative. We could either perform a phase resolved analysis, assuming a convective velocity equal to the organised velocity value at the phase under study (but some problems arise due to the short time series), or assume that the equivalent convective velocity is related to the velocity scale of the eddies (as we do in present analysis). Note that, in the present experiments, the ratio between the two different velocity scales used for micro and macro vortices is almost uniform along the vertical and the choice of one of the two scales
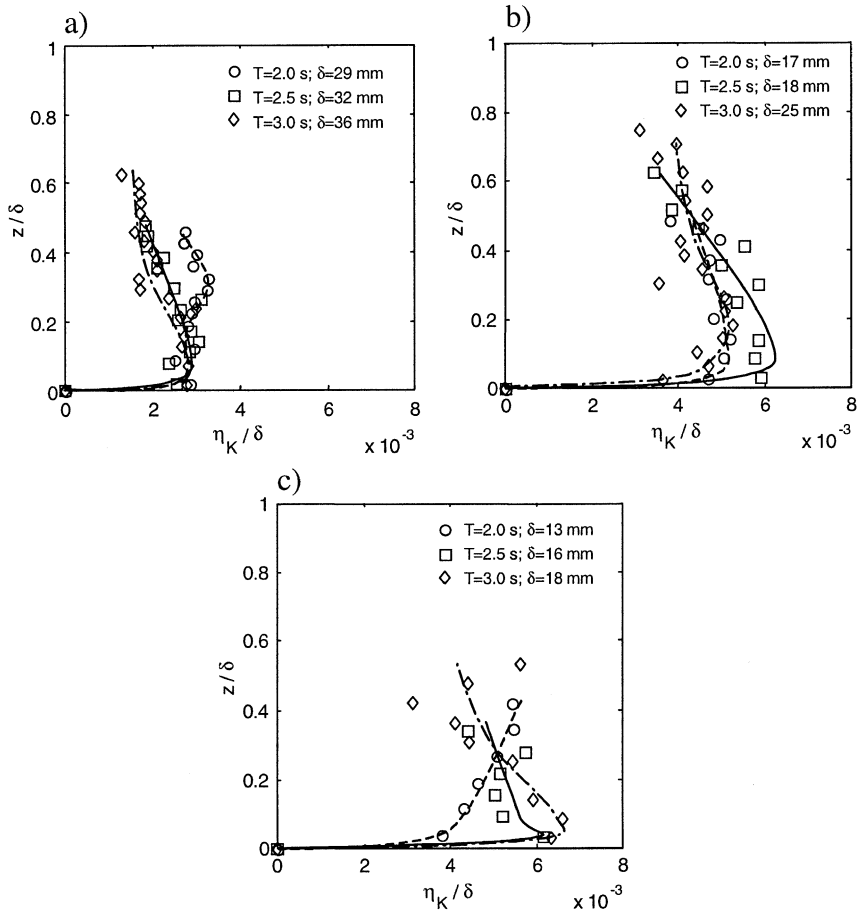
Fig. 18. Kolgomorov length micro scale η_K vs. height level estimated for all waves: (a) lower section (7), (b) mid section (8) and (c) upper section (9).

does not affect the shape of the vertical profile of length scales.

The micro scales can also be evaluated assuming that most energy is dissipated by viscosity acting efficiently in dampening micro vortices. If ε is the rate of dissipation, using a dimensional concept, the scale of dissipation is $\eta_K \equiv (\nu^3/\varepsilon)^{1/4}$; it is often referred to as the Kolgomorov length micro scale. The dissipation rate can be obtained by integrating the spectrum of dissipation or assuming that the dissipation is locally balanced by generation due to vortices:

$$\varepsilon \approx \frac{\left(\left\langle \sqrt{\widetilde{u'^2}} \right\rangle \right)^3}{\Lambda}. \tag{17}$$

The profiles are reported in Fig. 18. The trend is similar to that of the macro scale, as expected considering the relation (Tennekes and Lumley, 1972):

$$\frac{\eta_K}{\Lambda} = K^{-1/4} \mathrm{Re}_\Lambda^{-3/4}. \tag{18}$$

where $K \approx 1$ and $\mathrm{Re}_\Lambda = (u'\Lambda)/\nu$.

In Fig. 19 the eddy viscosity is shown based on Eq. (10) and is much higher than the eddy viscosity obtained in a uniform stream of equivalent depth and friction velocity. The latter is usually assumed to be parabolic:

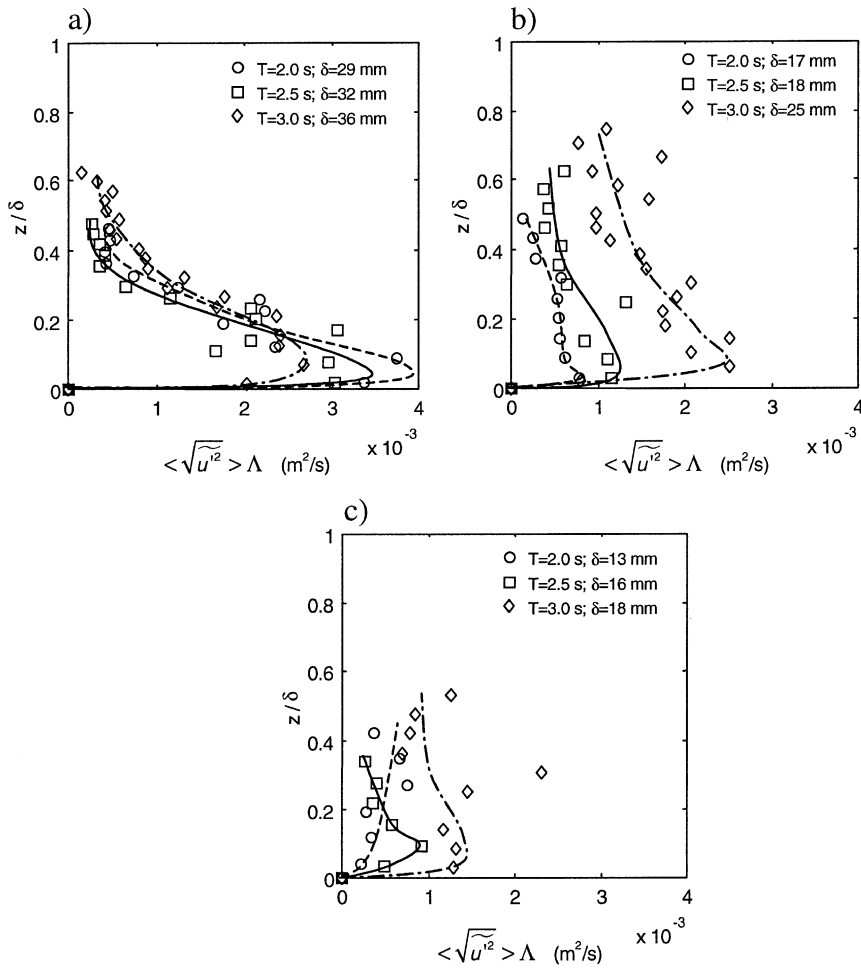$$\nu_t = k u_* z \left(1 - \frac{z}{\delta} \right), \tag{19}$$

Fig. 19. Coefficient of eddy diffusion as a function of the non-dimensional height level estimated for all waves: (a) lower section (7), (b) mid section (8) and (c) upper section (9).

where u_* is the friction velocity and k is the Von Karman coefficient. The friction velocity computed using the first level measurements ($z = 0.5$ mm) is on the order of 5 cm/s; thus the eddy viscosity in the equivalent uniform stream in an open-channel flow has a maximum in the middle equal to $\sim 1.3 \times 10^{-4}$ m^2/s, an order of magnitude smaller than the values sketched in Fig. 19. The mixing level is high and the consequence is an almost uniform velocity profile: momentum exchange is very efficient and possible deviations from a uniform velocity are smoothed very quickly. It is important to remember that from a phenomenological point of view, eddy viscosity related to vertical mixing is the product of vertical fluctuating velocity (or an estimator) and a proper vertical length scale; the assumption of equal vertical and horizontal length scales is certainly not satisfied near the bottom and the free surface, where vortices are stretched and interact with the boundaries.

A different approach to turbulence dynamics description is the spectral analysis of fluid velocity. Spectral analysis is the decomposition of a function into components of different wave number or frequency, and is an excellent tool to analyse energy transfer among the various components. The best

known spectrum is the Kolgomorov energy spectrum in the wave number domain:

$$E(k) = \alpha \varepsilon^{2/3} k^{-5/3}, \tag{20}$$

valid in the inertial sub-range, where $\alpha \approx 1.5$ and $k = 2\pi/L$. The inertial sub-range exists only if the Reynolds number Re_Λ is high enough, that is at least 10^5.

The Eulerian frequency spectrum is defined as:

$$S(f) = 4\widetilde{\langle u'^2 \rangle} \int_0^{+\infty} R_E(\tau)\cos(f\tau)\,d\tau; \tag{21}$$

The transformation between frequency and wave domain is assumed to be linear:

$$2\pi f = Uk \tag{22}$$

where U has been chosen as equal to the macro scale velocity (large-scale normalisation), with acceptable accuracy except in the productive sub-range $k\Lambda < 1$.

The obtained averaged spectrum is intrinsically weighted with the permanence time of the eddies in the flow field (turbulence is time varying). A possible effect of the time variation in turbulence is an exponential decay of the spectrum for wavenumber approaching zero if larger eddies (more efficient in extracting energy from mean flow) are dominant; an exponential decay of the spectrum for wave number approaching infinity if smaller eddies (more efficient in dissipation) are dominant (Tennekes and Lumley, 1972).

Some results are shown in Fig. 20, compared to Von Karman's spectrum of the form:

$$\frac{S(f)}{4\widetilde{\langle u'^2 \rangle}T_E} = \left(1 + (fT_E)^2\right)^{-5/6}; \tag{23}$$

that approaches the Kolgomorov $-5/3$-power law (equilibrium spectrum) as f becomes sufficiently large.

The estimated spectral distribution has the typical shape of the longitudinal equilibrium spectrum of fields of isotropic simple waves with waves of a different wave number, even though in the present experiments the turbulence field it is not isotropic especially near the bottom. The equilibrium spectrum is obtained in the hypothesis of infinite Reynolds number and of a local balance between production and dissipation. For low Reynolds number, the spec-

trum is deformed as qualitatively reported in Fig. 20a. The effects of a dominant production of turbulent energy are equivalent to an exponential decay of the spectrum in the low frequency range (Tennekes and Lumley, 1972) and are also qualitatively sketched in Fig. 20a. In the present tests both low Reynolds number ($Re < 10^3$) effects and turbulent energy production effects overlap and the inertial sub-range is almost non-existent.

There are essentially two layers characterised by a gradually varying spectrum shape; turbulence near
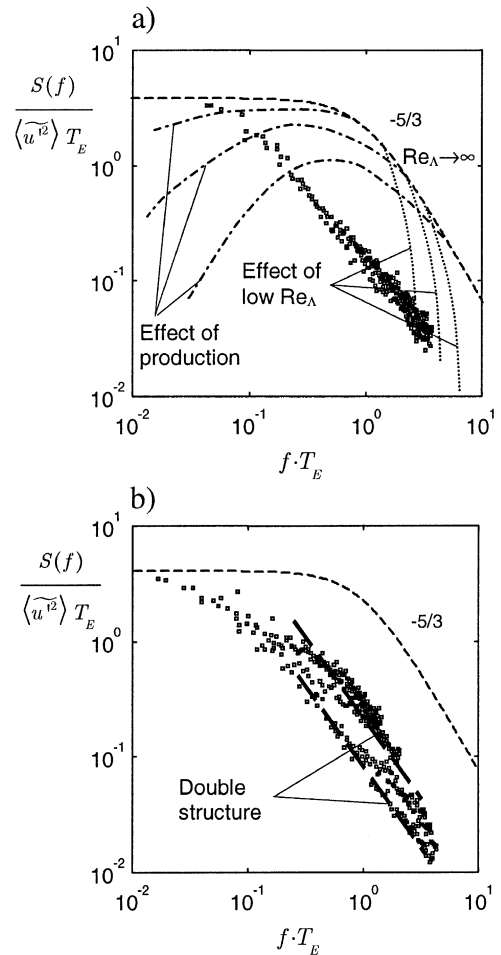

Fig. 20. Spectral densities of turbulent velocity $u'(z,t)$ in the upper section (9); test with period $T = 3$ s: (a) $z \leq 7.5$ mm; (b) $8.5 \leq z \leq 22.5$ mm. In (a) dashed line is the Von Karman's spectrum, dot lines represent the same spectrum for limited Reynolds number (increasing from left). Dash-dot lines represent the spectrum in presence of production of turbulent energy.

the bottom is decidedly non-isotropic whereas at the upper height level turbulence recovers partial isotropicity. A double structure can be observed in the upper section, upper layers (Fig. 20b). According to Monin and Yaglom (1975), the double structure of the spectrum is due to the presence of a double influx of external energies, and is usually recorded in many geophysical flows; the secondary source must have different characteristics from the main source in order to be detectable in the spectrum. We can infer that in the present test the secondary source is the back flow bore, developing with different characteristics to the uprush turbulent source. Generally speaking the situation is very different from conditions appropriate for the application of equilibrium concepts.

6. Conclusion

An extensive analysis of free surface and wave front characteristics, fluid velocity and turbulence in the swash zone generated by plunging and collapsing breaking has been presented.

During breaking, the presence of a jet rebounding after splash increases the run-up relative to the predicted run-up computed using simple kinematic concepts.

The measured fluid velocity is almost uniform over depth for most phases of motion.

Turbulent energy is much higher during uprush than during backrush. The Kolgomorov length micro scales, inversely related to turbulent energy dissipation, are smaller near the free surface and increase towards the bottom (an opposite trend is typical of open-channel flows, where dissipation is more important near the bottom).

Turbulent energy flux is essentially directed shore-ward.

The length macro scales, a measurement of the average size of the eddies in the production range, have a maximum near the bottom at $z/\delta \approx 0.1$, rapidly decreasing towards the free surface and the wall. Presumably, it is the source of turbulent energy near the free surface that is responsible for the inverted profile in respect to the same profile in an open-channel flow.

The equivalent steady eddy viscosity, as estimated from the horizontal integral length scale and horizontal turbulent velocity scale, again has a maximum at the same level $z/\delta \approx 0.1$, indicating a more efficient turbulent mixing near the bottom than near the free surface. The mean value of the eddy viscosity is one order of magnitude higher than the equivalent eddy viscosity in an open-channel flow of equal friction velocity. However, it is comparable with the values obtained by Pedersen et al. (1998), even though those values were obtained by measuring spatial correlations in the vertical for the vertical velocity component.

The Eulerian time spectrum shows a typical $-5/3$ slope at high frequency, but exhibits all the features of the low Reynolds number. The spatial evolution in the horizontal is almost undetectable in the three sections of measurements. A quite evident difference can be seen in the vertical, with a substantial two-layer structure. For the 3-s wave period in the upper section, a double structure is evident, probably due to two sources of turbulent energy.

Symbol	Unit	Description
ϑ		Bottom slope
$\langle u \rangle$	m/s	Mean velocity
u'	m/s	Fluctuating velocity
u''	m/s	Organised fluctuating velocity
η	m	Surface level
$\sim$		Phase or ensemble average operator
$\wedge$		Phasic average operator
$\langle \ \rangle$		Time average operator
ρ	kg/m^3	Mass density
ν	m^2/s	Kinematic fluid viscosity
Λ	m	Integral length scale of turbulence
δ	m	Maximum local water depth
λ	m	Taylor length micro scale
ε	m^2/s^3	Turbulent energy dissipation rate
κ	m^2/s^2	Turbulent kinetic energy
α, K		Coefficients
ξ_b, I_b		Surf similarity parameters
τ_E	s	Eulerian time micro scale

Symbol	Unit	Description
η_{K}	m	Kolgomorov length micro scale
ν_{T}	$\mathrm{m^2/s}$	Turbulent eddy viscosity
a_{f}	$\mathrm{m/s^2}$	Front acceleration
$E(k)$	$\mathrm{m^3/s^2}$	Energy spectrum
f	Hz	Frequency
g	$\mathrm{m/s^2}$	Gravitational acceleration
H_0, H_1	m	Wave height in deep water, at Section 1
k	$\mathrm{m^{-1}}$	Wave number
$\boldsymbol{k}$		Von Karman coefficient
L	m	Length scale, wave length
LDV		Laser Doppler Velocimetry
L_0	m	Wave length in deep water
N		Number of samples
p	Pa	Pressure
$R(r)$		Normalised Space autocorrelation
Re_Λ		Reynolds number based on integral turbulence length scale
$R_{\mathrm{E}}(\tau)$		Normalised Eulerian time autocorrelation
R_{u}	m	Run-up
$S(f)$	$\mathrm{m^2/s}$	Eulerian frequency spectrum
T	s	Wave period
T_{m}	s	Period of time averaging
t, t^*, τ	s	Time variable
T_{E}	s	Time macro scale of turbulence
U	m/s	Velocity scale
u_*	m/s	Friction velocity
U_{f}	m/s	Front velocity
x, y, z, x_i	m	Spatial coordinates

Acknowledgements

References

Battjes, J.A., Sakai, T., 1980. Velocity field in a steady breaker. J. Fluid Mech. 111, 421–437.

Blackwelder, R.F., Kaplan, R.E., 1976. On the wall structure of the turbulent boundary layer. J. Fluid Mech. 76, 80–112.

Gourlay, M.R., 1992. Wave set-up, wave run-up and beach water table: interaction between surf zone hydraulics and groundwater hydraulics. Coastal Eng. 17, 93–144.

Hussain, A.K.M.F., 1983. Phys. Fluids 26, 2816.

Kozakiewicz, A., Sumer, B.M., Fredsøe, J., Deigaard, R., 1998. Effect of external generated turbulence on wave boundary layer. Report No. 77, Inst. of Hydrodynamics and Hydraulic Engineering, ISVA, Techn. Univ. Denmark.

McComb, W.D., 1990. The Physics of Fluid Turbulence. Oxford Univ. Press, Oxford.

Monin, A.S., Yaglom, A.M., 1975. Statistical Fluid Mechanics, vol. 2. MIT Press, Cambridge, MA.

Nadaoka, K., Hino, M., Koyano, Y., 1989. Structure of the turbulent flow field under breaking waves in the surf zone. J. Fluid Mech. 204, 359–387.

Nezu, I., Nakagawa, H.I., 1993. Turbulence in open channel flows. IAHR Monogr. Ser.

Papoulis, A., 1965. Probability, Random Variables and Stochastic Problems. McGraw-Hill, New York.

Pedersen, C., Deigaard, R., Sutherland, J., 1998. Measurements of the vertical correlation in turbulence under broken waves. Coastal Eng. 35, 231–249.

Peregrine, D.H., 1983. Breaking waves on beaches. Ann. Rev. Fluid Mech. 15, 149–178.

Peregrine, D.H., Svendsen, I.A., 1978. Spilling breakers, bores and hydraulic jumps. Proc. 16th Int. Conf. Coastal Eng., pp. 540–550.

Petti, M., 1988. Second order analysis of shallow-water spectra. Il Nuovo Cimento 11C, N5–N6.

Petti, M., 1994. Third-order analysis of non-linearities bounded to narrow banded spectra. J. Offshore Polar Eng. 4 (4), 257–264.

Petti, M., Longo, S., Sadun, S., Tirindelli, M., 1998. Swash zone hydrodynamics on a 1:10 bottom slope: laboratory data. SASME Report FIUD-01-98, Univ. of Florence.

Resh, F.J., Leutheusser, H.J., 1972. Reynolds stress measurements in hydraulic jumps. J. Hydraul. Res. 10, 409–430.

Rodriguez, A., Sanchez-Arcilla, A., Redondo, J.M., Mosso, C., 1999. Macroturbulence measurements with electromagnetic and ultrasonic sensors: a comparison under high-turbulent flows. Exp. Fluids 27, 31–42.

Shen, M.C., Meyer, R.E., 1963. Climb of a bore on a beach: Part 3. Run-up. J. Fluid Mech. 16, 113–125.

Stive, M.J.F., 1980. Velocity and pressure field of spilling breakers. Proc. ICCE, ASCE, 547–566.

Stoker, J.J., 1957. Water Waves. Wiley, New York.

Tennekes, H., Lumley, J.L., 1972. A First Course in Turbulence. The MIT Press, Cambridge, MA.

Telionis, P.D., 1981. Unsteady viscous flows, Spring Series in Computational Physics. Springer-Verlag.

Ting, C.K.F., Kirby, J.T., 1994. Observation of undertow and turbulence in a laboratory surf-zone. Coastal Eng. 24, 51–80.

Ting, C.K.F., Kirby, J.T., 1995. Dynamics of surf-zone turbulence in a strong plunging breaker. Coastal Eng. 24, 177–204.

Ting, C.K.F., Kirby, J.T., 1996. Dynamics of surf-zone turbulence in a spilling breaker. Coastal Eng. 27, 131–160.

Yeh, H.H., Ghazali, A., Marton, I., 1989. Experimental study of bore run-up. J. Fluid Mech. 206, 563–578.